

Supporting Information

Structural Dynamics upon Photoexcitation in a Spin Crossover Crystal Probed with Femtosecond Electron Diffraction

*Yifeng Jiang, Lai Chung Liu, Henrike M. Müller-Werkmeister, Cheng Lu, Dongfang Zhang, Ryan L. Field, Antoine Sarracini, Gustavo Moriena, Eric Collet, and R. J. Dwayne Miller**

anie_201702497_sm_miscellaneous_information.pdf

Author Contributions

Y.J. Conceptualization: Equal; Formal analysis: Supporting; Investigation: Equal; Methodology: Equal; Writing – original draft: Lead; Writing – review & editing: Supporting

L.L. Formal analysis: Lead; Software: Lead; Writing – original draft: Equal; Writing – review & editing: Supporting

H.M. Conceptualization: Supporting; Funding acquisition: Supporting; Investigation: Supporting; Methodology: Supporting; Writing – original draft: Equal; Writing – review & editing: Lead

C.L. Methodology: Supporting

D.Z. Data curation: Supporting; Methodology: Supporting

R.F. Data curation: Supporting; Investigation: Supporting; Writing – original draft: Supporting

A.S. Investigation: Supporting; Methodology: Supporting

G.M. Formal analysis: Supporting; Methodology: Supporting; Writing – original draft: Supporting

E.C. Conceptualization: Supporting; Resources: Supporting; Writing – review & editing: Supporting

D.M. Conceptualization: Equal; Funding acquisition: Lead; Resources: Lead; Writing – review & editing: Supporting.

Supplementary Information

Contents

1. Crystal information

1.1 Crystal structure

1.2 Magnetic Susceptibility, XANES and Optical Transmission vs. Temperature

2. Experimental Conditions

2.1 Temporal Resolution Measurement

2.2 Excitation Fraction Calculation

3. FED Data Collection

4. Fluence Dependence

5. FED Data Analysis

5.1 Orientation Determination and Indexing

5.2 Simulation of Diffraction and Difference Patterns

6. Time Constant Calculation

6.1 Global Fitting of Time-dependent Diffraction Intensity

7. Time-dependent Model of Atomic Motions

References

1. Crystal information

1.1 Crystal Information

The single crystal of $[\text{Fe}(\text{PM-AzA})_2](\text{NCS})_2$ was prepared by Létard, J. F. *et al.*^[1] Guionneau *et al.*^[2] used X-ray diffraction to obtain the single crystal structure of the Fe(II) spin crossover (SCO) compound $[\text{Fe}(\text{PM-AzA})_2](\text{NCS})_2$ (cis-bis(thiocyanato)-bis(N-2'-pyridyl-methylene)-4-(phenyl-azo) aniline iron(II)). The low spin (LS) and the high spin (HS) structures were collected at 110K and 295K, respectively. Key crystal information is summarized in Table S1.^[3]

Ultra-microtomy is used to cleave the single crystal of $[\text{Fe}(\text{PM-AzA})_2](\text{NCS})_2$ to be 150 nm thick. This thickness is optimized to obtain diffraction patterns by electron diffraction in transmission mode at 95 kV. The crystals were picked by from the water surface by standard TEM cooper meshes. The typical size of the crystals on the TEM meshes was 1 mm×500μm×150nm.^[4]

Table S1: Single crystal information of $[\text{Fe}(\text{PM-AzA})_2](\text{NCS})_2$ at different temperature

Temperature (K)	110 K	295 K
Crystal system	Monoclinic	Monoclinic
Space group	P 21/c	P 21/c
a (Å)	15.038	15.155
b (Å)	14.396	14.623
c (Å)	16.677	17.068
α (deg)	90	90
β (deg)	92.84	92.95
γ (deg)	90	90
V (Å ³)	3605.92	3777.45
Fe-N bond (Å)	1.97	2.16
Fe atom fraction	(0.291 0.284 0.068)	(0.292 0.287 0.055)

From the LS state to the HS state, crystal system and space group are still same, so there is no appearance or disappearance of diffraction peaks during the SCO. The structural motions in the

local FeN_6 octahedron is the elongation of six Fe-N bonds and the distortion of the N-Fe-N angles as the consequence of ligand motion. The average Fe-N bond distance increases $\sim 0.2 \text{ \AA}$ from LS to HS which is considered as a key structure signature of SCO process in FeN_6 environment^[3].

1.2 Magnetic Susceptibility, XANE and Optical Transmission vs. Temperature

$[\text{Fe}(\text{PM-AzA})_2](\text{NCS})_2$ has both thermal SCO and photo induced SCO.^[5,6] The thermal SCO of $[\text{Fe}(\text{PM-AzA})_2](\text{NCS})_2$ has been monitored by magnetic susceptibility, X-ray absorption at 7125 eV and optical reflectivity in Figure S1.^[5] Those methods show $[\text{Fe}(\text{PM-AzA})_2](\text{NCS})_2$ crystals undergo a smooth isostructural spin crossover with $T_{\frac{1}{2}} = 184 \text{ K}$, a typical of non cooperative system. In our FED experiment, 25% samples are HS state and 75% samples are LS state at 170 K.^[6]

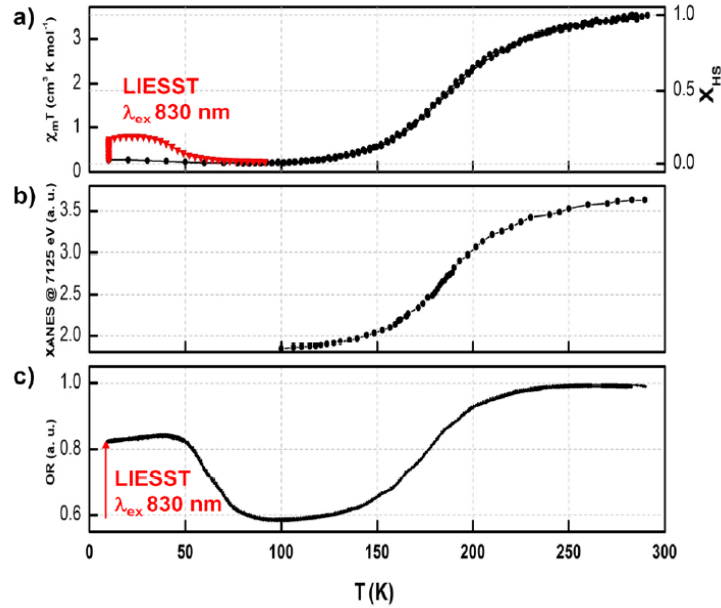


Figure S1: Temperature dependence of (a) $\chi_M.T$ (b) XANES (c) optical reflectivity for spin crossover of the $[\text{Fe}(\text{PM-AzA})_2](\text{NCS})_2$. Reprinted with permission from [5] ©2015 Eric Collet, *et al.*

2. Experimental Conditions

In this study, a 95 keV hybrid DC-RF electron source is employed to generate femtosecond electron pulses as an ultrafast structural probe. Time resolution and space resolution of the electron source have been described and characterized in recent studies.^[4] Figure S2 shows the schematic diagram of the FED setup used in this work. We generate 5.3×10^4 electrons per pulse with a spot size of $(275 \pm 20) \mu\text{m}$ diameter ($0.86 \text{ e}^-/\mu\text{m}^2$), a repetition rate of 100 Hz and 0.5 % electron shot to shot intensity stability.

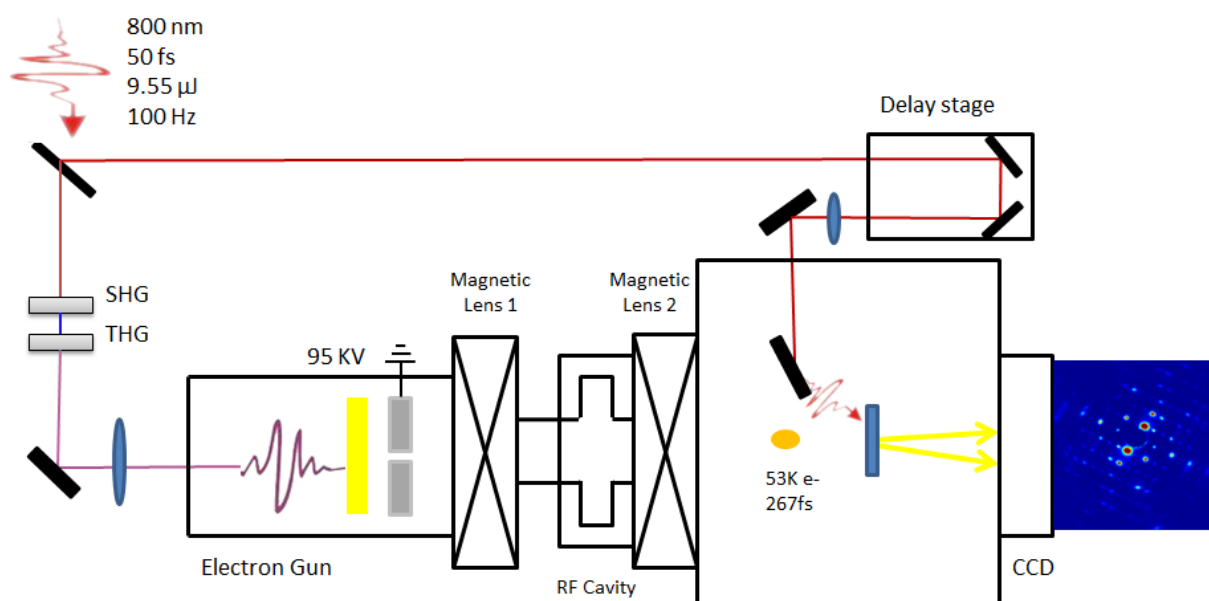


Figure S2: Schematic diagram of the FED setup. FED is a classic pump probe experiment. In the experiment, femtosecond laser is applied to excite the sample as pump and generate femtosecond electron pulses as the probe. At the sample position, the arrival time of the pump laser (transversal diameter 550 μm FWHM, 9.55 μJ and centered at 800 nm) and the probe electron beam (53 k e⁻ and 275 μm FWHM transversal size, 267 fs FWHM pulse duration) is synchronized. By changing the delay time of pump laser, the transient structural information can be collected by CCD.

2.1 Temporal Resolution Measurement

One of the most important features of FED experiment is the femtosecond pulse duration of electron beams which has enough temporal resolution to study ultrafast atom motions. One of the advantages of DC-RF electron sources is that the brightness of the electron beam is somewhat higher than that of regular DC electron sources, and the distance between the photocathode in the electron gun and the sample position in the sample chamber can be much larger than that in regular DC electron sources. This DC-RF design gives more space for an additional cold finger and a rotation stage for different experiments.

In our hybrid DC-RF electron source, the pulse duration is the key parameter, which needs to be confirmed before the pump probe experiment. RF can recompress pulse duration of ultrabright electron beams in the sample position to ~ 300 fs.^[4f] Our group has applied multiple techniques to measure electron pulse durations such as ponderomotive scattering,^[7,8] time constant measurements of the electron- phonon relaxation process in Si^[9] and streak camera.^[10,11] In this experiment, the streak camera method was employed to measure the electron pulse duration before every pump-probe experiment, to ensure that the RF field amplitude applied to RF cavity is optimized for the different intensities of the electron beams.

In streak camera measurements, the electron beam is deflected in the transverse direction on the CCD by a pair of streak plates with a time dependent electric field. The magnitude of the deflection is proportional to its arrival time to the streak plates, so the velocity profile of electron beam is displayed across the CCD.^[10,11] By measuring the magnitude of the deflection on CCD, pulse durations can be obtained. The electron pulse duration can be calculated based on following equation:^[10]

$$W_{str}^2 = W_{un}^2 + K_s^2 \Delta\tau_e^2 \quad (S1)$$

Where W_{str} is FWHM of streaked beam; W_{un} is FWHM of unstreaked beam; K_s is the streak velocity (SV); $\Delta\tau_e$ is the pulse duration of electron beam. Therefore, the electron pulse duration

can be obtained given K_s , W_{str} and W_{un} . Figure S3a shows the relation between the electron pulse duration and RF field amplitude. In order to keep a small transverse beam size and obtain the best pulse duration, the temporal focus at the sample position is attained with an RF field amplitude between 1.6 MV/m to 1.75 MV/m. Therefore, in the experiment, the RF field amplitude was set to 1.68 MV/m to obtain the shortest and most stable pulse duration. In Figure S4, we also increased the streak velocity by increasing the voltage on the streak plates, noting that the electron pulse duration stayed around 180 fs FWHM.

In the DC-RF hybrid electron gun used in these experiments, the measured temporal IRF has contributions from both the arrival time jitter 200 fs RMS (Figure S3b) and the pulse duration of single electron beam 178 fs FWHM (Figure S3a) based on 63 pixel/ps streak velocity. Thus, the electron pulse duration of is 267 fs FWHM. The time resolution could be improved by time stamping but as seen below (section 5), the signal to noise and this temporal instrument response function was sufficient to resolve the key motions.

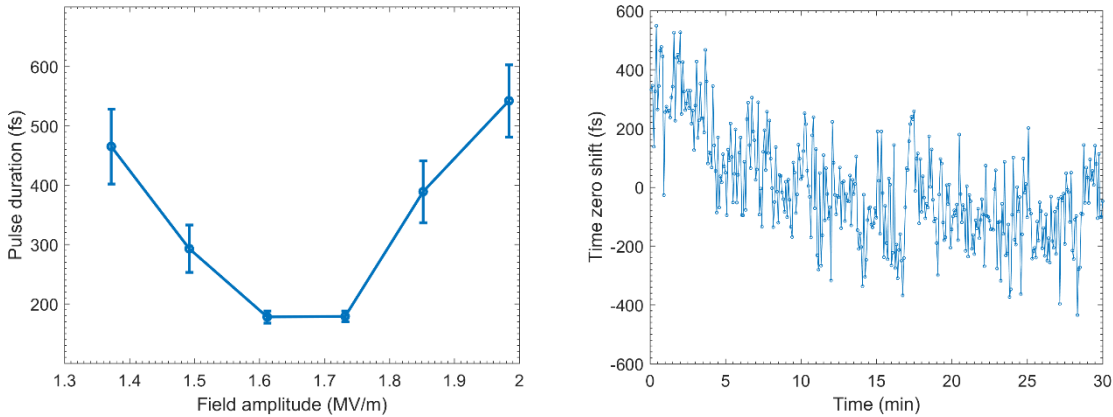


Figure S3: Pulse duration measurement. a) Pulse duration measured by streak camera vs. RF field amplitude. Shortest pulse duration is 178 fs FWHM. b) Single shot electron time zero shift vs time. The jitter is 200 fs RMS.

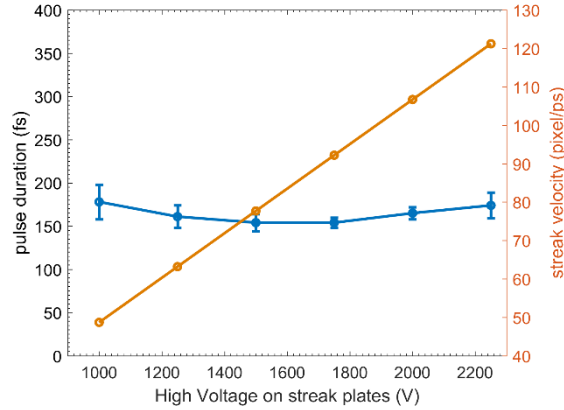


Figure S4: Streak velocity vs pulse duration of single electron beam. The electron pulse duration remains approximately 180 fs FWHM at different streak velocities.

The sample was mounted on copper TEM grid and connected to a liquid nitrogen cold finger. The equilibrium temperature of the sample was measured to be (170 ± 5) K. At this temperature, 25% of molecules in the crystal are at high spin state and 75% of molecules are at low spin state.

2.2 Excitation Fraction Calculation

To investigate the SCO dynamics of $[\text{Fe}(\text{PM-AzA})_2](\text{NCS})_2$, we employed 60 fs pump pulses centered at 800 nm. At the sample position, the pulse energy was (9.55 ± 0.05) μJ per pulse and the laser beam diameter was (550 ± 20) μm . The incident excitation fluence was 1.28 mJ/cm^2 . We measured the transmission of the pump laser to be $(38 \pm 2)\%$ at 170 K. The excitation fraction is 12.5% based on the number of absorbed photons and molecules in the crystal.

In order to confirm excitation fraction which is critical for further data analysis, we applied another two calculations of the excitation fraction from electron diffraction signal beside excitation fraction obtained from laser excitation conditions.

First, the excitation fraction can also be calculated:^[4]

$$\eta_{exc} = \frac{F_{exp}(k, t_{\infty}) - F(k)}{F_{HT}(k) - F(k)} \quad (\text{S2})$$

η_{exc} is the excitation fraction; F_{LS} is the structure factor of low spin state; F_{HS} is the structure factor of high spin state. We assume the system has reached HS excited state after 10 ps and starts to have phonons oscillation at 20 ps. Therefore, we take $t_{\infty} = 10 \text{ ps} < t < 20 \text{ ps}$. A distribution of excitation fractions is expected, because η_{exc} obtained by this equation is sensitivity to the signal to noise of every diffraction peak. Figure S5 shows the calculated excitation fractions of selected 26 diffraction peaks. The mean of excitation fraction is 13.5% which is consistent with the above independent determination.

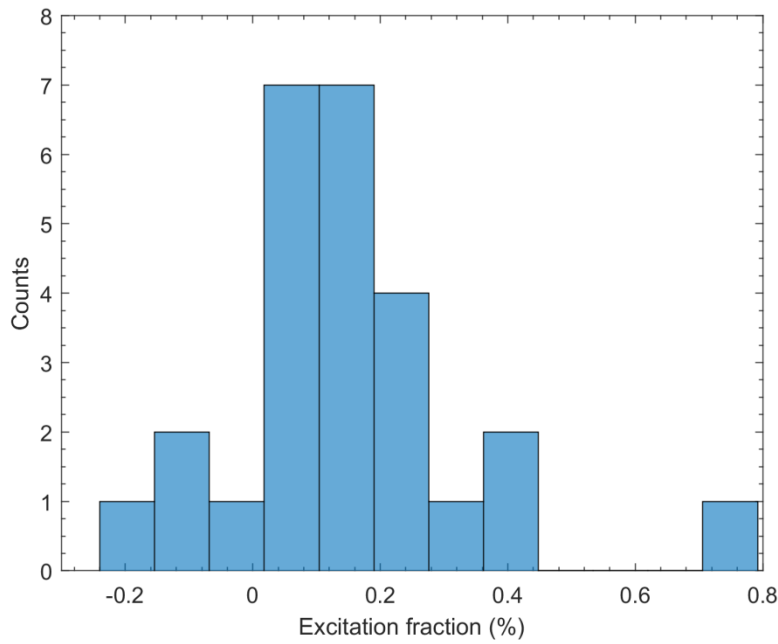


Figure S5: Distribution of excitation fractions of selected 26 diffraction peaks

3.FED Data Collection

Diffraction images were collected with an exposure time of 0.2 seconds at 100 Hz (20 electron pulses) to avoid saturation of peak (0 0 0) on CCD and make sure samples can recover from last excitation before next pump laser. SCO electron diffraction signal $((I_{\text{on}} - I_{\text{off}})/I_{\text{off}})$ is only sub 3%, so it is necessary to improve electron shot to shot stability. In the experiment, pinhole size on the anode in electron gun was decreased from 500 μm to 200 μm to saturate output brightness of electron beam. Therefore, shot to shot electron intensity stability was measured to be sub 0.5%. Although intensity of 270 nm laser which is applied to generate electron beams may change

during the experiment, brightness of electron beam is still stable. To optimize the ultrafast time trace, every time step of the time traces was repeated using 250 diffraction images. Therefore, the final time trace is an average of 5000 pulses per time point.

4. Fluence Dependence

We measured the fluence dependence of our sample for excitations from 0.93 mJ/cm² to 1.38 mJ/cm². We tried higher than 1.38 mJ/cm² fluence and found a slow decrease of the intensity of diffraction peaks in 3 hours, which indicates damage to the sample. On the other hand, the diffraction peaks' intensity does not show signs of damage after weeks of experiment when the fluence is lower than 1.28 mJ/cm². Figure S6 shows the selected peaks' normalized averaged signals between 10 ps and 20 ps as a function of the fluence. The fluence we used in the reported experiments is in the linear range of the plot.

Figure S6 and Figure S7 show selected peaks' change while pump fluence increasing.

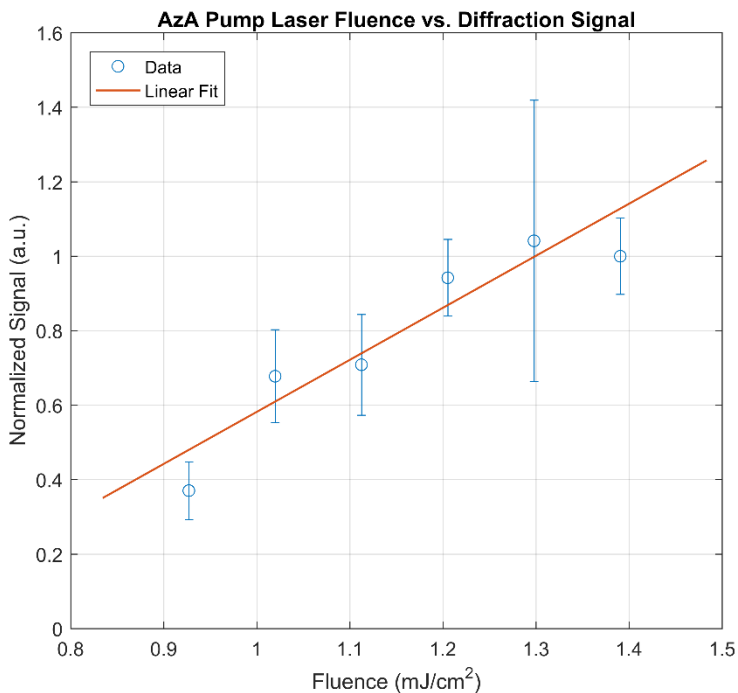


Figure S6: Summary of fluence dependence of [Fe(PM-AzA)₂](NCS)₂

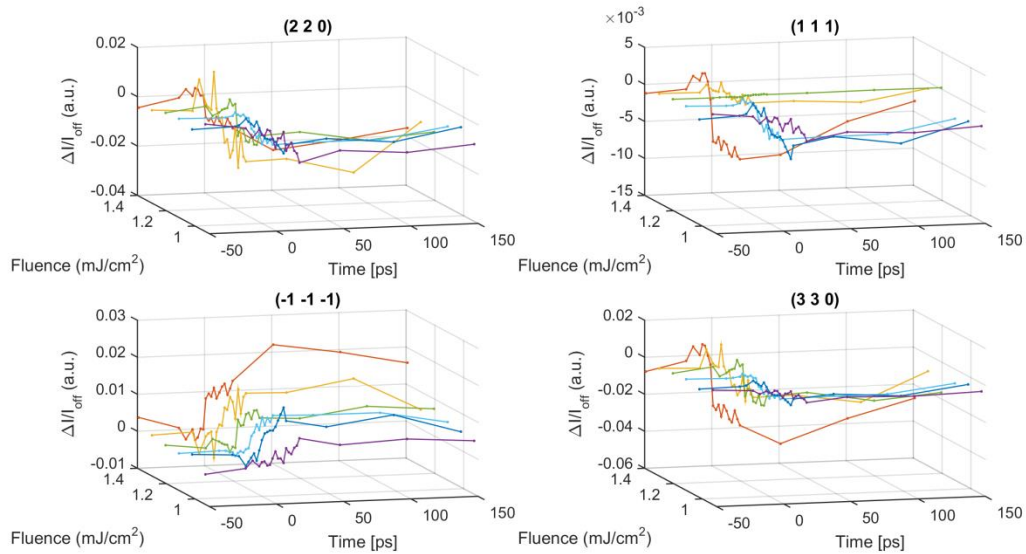


Figure S7: Fluence dependence of selected diffraction peaks

5. FED data analysis

5.1 Orientation determination and indexing

A first step to analyzing diffraction data is the determination of the crystal orientation of the sample, which is also the incident direction of the probing electron beam. Here, we simulate the electron diffraction pattern of the sample over 8 parameters and compare it with the experimental data at $T = 300$ K to find the best fit. These parameters are: camera parameter, 3 Miller indices, sample thickness, overall coherence length, in-plane sample rotation, Debye-Waller factor.

The camera parameter is the conversion factor between the local coordinate system on the camera sensor to the absolute coordinates in reciprocal space. The 3 Miller indices determine the relative direction of the incident vector to the reciprocal unit vectors. The sample thickness and overall coherence length are modelled using a Gaussian shape function to the reciprocal lattice points; they are the inverse of the width along the parallel and perpendicular direction to the incident vector, respectively. In-plane sample rotation refers to the rotation around the incident direction. The Debye-Waller factor is taken into account as a Gaussian pre-factor that attenuates the magnitude of the structure factors at higher scattering angles. Figure S8 shows the result of the refinement process.

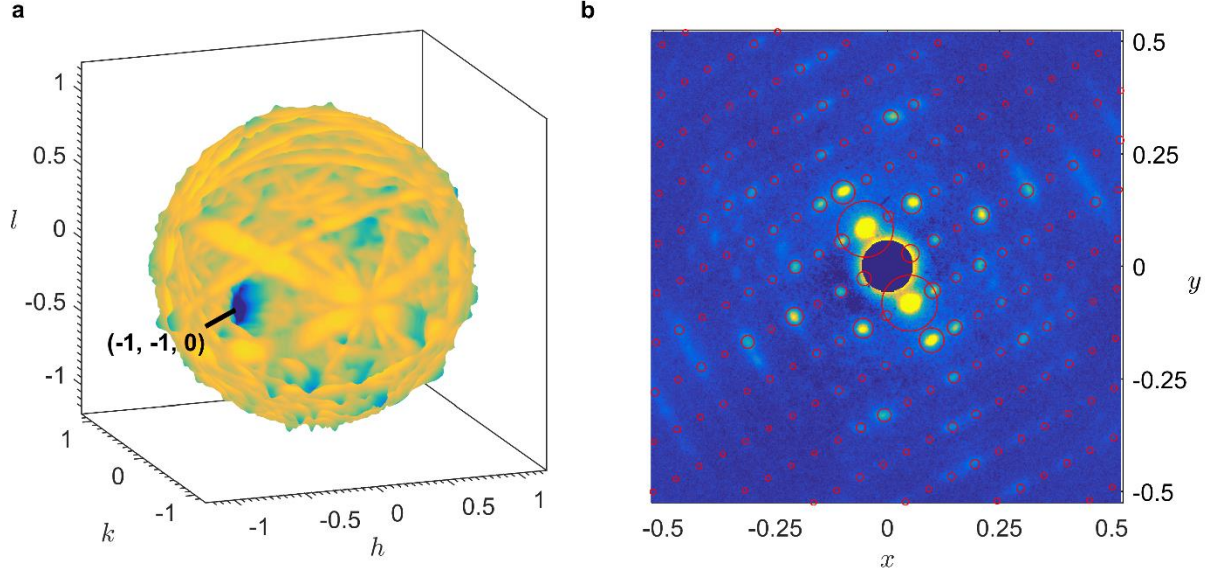


Figure S8: Refinement of Crystal Orientation. a, Spherical plot of the Pearson correlation coefficient for refining the crystal orientation of the sample with respect to the crystallographic axes; the blue region centered around (-1 -1 0) shows the area of best fit. b, Electron diffraction pattern at 300 K is overlaid with simulated data using best-fit parameters.

5.2 Simulations of structural factor

Previous studies^[12-18] suggest that Fe-N elongation, which happens simultaneity with spin crossover should be finished in sub-150 fs. Therefore, it is important to confirm whether our FED has enough space and time resolution to observe ~ 0.2 Å Fe-N bond elongation on the sub 150 fs time scale and what kind of electron diffraction signal we would expect to observe if Fe-N bond elongation happens in sub 150 fs and following with ligand motion and unit cell expansion in 2 ps.

The intensity changes of diffraction peaks are associated with motions of atoms in the SCO process by increase or decrease interferences of electrons. Structure factors (F) can indicate these changes, because the position (xyz) of atom j within the unit cell determines the intensity of a diffraction peak, which is proportional to the square of the structure factor.^[19]

$$I(hkl) \propto |F(hkl)|^2 \quad (\text{S3})$$

Therefore, the intensity changes noted in diffraction patterns in FED can be simulated based on structure factor changes from motions in the unit cell.

In this study, the kinematic theory was applied for electron diffraction to calculate the diffraction patterns.^[19] Weak-phase-object approximation (WPO) needs to be considered to justify the use of kinematical theory over dynamical theory. Given FED experimental conditions, it is reasonable to employ the single scattering formulation for $[\text{Fe}(\text{PM-AzA})_2](\text{NCS})_2$ electron diffraction calculation:^[19]

$$F(k) = \sum_{j=1}^N f_j e^{2\pi i k \cdot r_j} \quad (\text{S4})$$

Where f_j is the atomic scattering factor for the j^{th} atom, parameterized as:^[19]

$$f_j(k) = \sum_{l=1}^5 a_l e^{\frac{1}{4} b_l k^2} \quad (\text{S5})$$

In order to simulate structure factor change of spin crossover, we employed the low spin structure at 110 K and the high spin structure at 300 K from the structure data base² to study the contribution from different motions in the SCO process. The intensity change in Bragg peaks can be used to follow the Fe-N bond elongation and ligand motion. Figure 5 in the main article shows the Bragg peak intensity change contribution (in percentage and indicated by different colors) to selected most intense diffraction peaks.

6. Time Constant Calculation

6.1 Global Fitting of Time-dependent Diffraction Intensity

In $[\text{Fe}(\text{PM-AzA})_2](\text{NCS})_2$ FED experiment data analysis, we found that there is only one process of structural change of photo excited spin crossover. To confirm this statement, we checked time constants for almost all bright diffraction peaks.

Of the hundreds of observable Bragg spots, we selected 30 representative ones that are bright and/or show strong pump-probe signal $\Delta I_i(t)$ where

$$\Delta I_i(t) = \frac{I_{i,ON}(t) - I_{i,OFF}(t)}{I_{i,OFF}(t)} \quad (\text{S6})$$

$I_{i,X}(t)$ is the intensity of diffraction peak i under pump state X at time t . These data points are then described using a global fitting model as follows:

$$S_i(t) = G_\sigma(t) * [c_i(1 - e^{-t/\tau})] = \frac{1}{2} c_i \left[\left(1 + \operatorname{erf} \left(\frac{t}{\sqrt{2}\sigma} \right) \right) - e^{-t/\tau} e^{\frac{1}{2} \left(\frac{\sigma}{\tau} \right)^2} \left(1 + \operatorname{erf} \left(\frac{t - \frac{\sigma^2}{\tau}}{\sqrt{2}\sigma} \right) \right) \right] \quad (\text{S7})$$

σ is the instrument response time (267 fs FWHM or 113 fs 1/e). By fitting all the data points simultaneously, we obtained a robust value for the time constant: $\tau = (2.32 \pm 0.09)$ ps.

7. Time-dependent Model of Atomic Motions

Electron diffraction is a direct probe of atomic positions. Here, we follow the motion of the atoms during the photochemical process using an approach similar to previous work on structure recovery from ultrafast electron diffraction data.^[4] A model is constructed by the atomic displacements parameterizing into 3 normalized variables (ξ_N, ξ_L, ξ_U that would link the LS and HS molecular structures within their respective crystallographic unit cell). For each time point measured in the experiment, a least square fitting routine is used to find the optimal set of parameters (i.e. reaction coordinates) that would best match the observed changes in diffraction intensity.

We defined these 3 reaction coordinates as follows:

- 1) Elongation of the 6 Fe-N bonds, collinear with the bond direction
- 2) Motion of the PM-AzA ligands, relative to the Fe atom position
- 3) Distortion of the crystallographic unit cell

The result of the fitting is a series of points in the 3D configuration space that best match the observations and trace out the entire reaction pathway from the initial LS structure to a final HS-like one.

Reference

- [1] J.-F. Létard, L. Capes, G. Chastanet, N. Moliner, S. Létard, J.-A. Real, O. Kahn, *Chem. Phys. Lett.* **1999**, 313, 115.
- [2] P. Guionneau, J.-F. Létard, D. S. Yufit, D. Chasseau, G. Bravic, A. E. Goeta, J. A. K. Howard, O. Kahn, *J. Mater. Chem.* **1999**, 9, 985.

- [3] Crystal information files of both states are downloaded from CCDC (Cambridge Crystallographic Data Centre).
- [4] M. Gao, C. Lu, H. Jean-Ruel, L. Liu, A. Marx, K. Onda, Sh.-y. Koshihara, Y. Nakano, X. Shao, T. Hiramatsu, G. Saito, H. Yamochi, R. R. Cooney, G. Moriena, G. Sciaini, R. J. D. Miller, *Nature* **2013**, 496, 343.
- [5] A. Marino, M. Cammarata, S. F. Matar, J.-F. Létard, G. Chastanet, M. Chollet, J. M. Glowonia, H. T. Lemke, E. Collet, *Struct. Dyn.* **2016**, 3, 023605.
- [6] A. Marino, M. Servol, R. Bertoni, M. Lorenc, C. Mauriac, J.-F. Létard, E. Collet, *Polyhedron*. **2013**, 66, 123.
- [7] C. T. Hebeisen, R. Ernstorfer, M. Harb, T. Dartigalongue, R. E. Jordan, R. J. D. Miller, *Opt. Lett.* **2006**, 31, 3517.
- [8] C. T. Hebeisen, G. Sciaini, M. Harb, R. Ernstorfer, T. Dartigalongue, S. G. Kruglik, R. J. D. Miller, *Opt. Express*. **2008**, 16, 3334.
- [9] M. Harb, W. Peng, G. Sciaini, C. T. Hebeisen, R. Ernstorfer, M. A. Eriksson, M. G. Lagally, S. G. Kruglik, R. J. D. Miller, *Phys. Rev. B*. **2009**, 79, 094301.
- [10] X. Wang, S. Nie, H. Park, J. Li, R. Clinite, R. Li, X. Wang, J. Cao, *Rev. Sci. Instrum.* **2009**, 90, 013902.
- [11] G. H. Kassier, K. Haupt, N. Erasmus, E. G. Rohwer, H. Schwoerer, *J. Appl. Phys.* **2009**, 105, 113111.
- [12] W. Zhang, R. Alonso-Mori, U. Bergmann, C. Bressler, M. Chollet, A. Galler, W. Gawelda, R. G. Hadt, R. W. Hartsock, T. Kroll, K. S. Kjær, K. Kubicek, H. T. Lemke, H. W. Liang, D. A. Meyer, M. M. Nielsen, C. Purser, J. S. Robinson, E. I. Solomon, Zh. Sun, D. Sokaras, T. B. van Driel, G. Vanko, T.-C. Weng, D. Zhu, K. J. Gaffney, *Nature* **2014**, 509, 345.
- [13] Ch. Bressler, C. Milne, V.-T. Pham, A. ElNahhas, R. M. van der Veen, W. Gawelda, S. Johnson, P. Beaud, D. Grolimund, M. Kaiser, C. N. Borca, G. Ingold, R. Abela, M. Chergui, *Science* **2009**, 323, 489.
- [14] H. T. Lemke, C. Bressler, L. X. Chen, D. M. Fritz, K. J. Gaffney, A. Galler, W. Gawelda, K. Haldrup, R. W. Hartsock, H. Ihee, J. Kim, K. H. Kim, J. H. Lee, M. M. Nielsen, A. B. Stickrath, W. Zhang, D. Zhu, M. Cammarata. *J. Phys. Chem. A*. **2013**, 117, 735.
- [15] K. Haldrup, W. Gawelda, R. Abela, R. Alonso-Mori, U. Bergmann, A. Bordage, M. Cammarata, S. E. Canton, A. O. Dohn, T. B. van Driel, D. M. Fritz, A. Galler, P. Glatzel, T. Harlang, K. S. Kjær, H. T. Lemke, K. B. Møller, Z. Németh, M. Pápai, N. Sas, J. Uhlig, D. Zhu, G. Vankó, V. Sundström, M. M. Nielsen, Ch. Bressler, *J. Phys. Chem. B* **2016**, 120, 1158.
- [16] M. Cammarata, R. Bertoni, M. Lorenc, H. Cailleau, S. D. Matteo, C. Mauriac, S. F. Matar, H. Lemke, M. Chollet, S. Ravy, C. Laulhé, J.-F. Létard, E. Collet, *Phys. Rev. Lett.* **2014**, 113, 227402.
- [17] E. Collet, M. Lorenc, M. Cammarata, L. Guérin, M. Servol, A. Tissot, M. Boillot, H. Cailleau, M. Buron-Le Cointe, *Chem. Eur. J.* **2012**, 18, 2051.
- [18] H. T. Lemke, K. S. Kjær, R. Hartsock, T. B. van Driel, M. Chollet, J. M. Glowonia, S. Song, D. Zhu, E. Pace, M. M. Nielsen, M. Benfatto, K. J. Gaffney, E. Collet, M. Cammarata, *Nat. Commun.* **2017**, 8, 15342.

- [19] E. Biasin, T. B. van Driel, K. S. Kjær, A. O. Dohn, M. Christensen, T. Harlang, P. Chabera, Y. Liu, J. Uhlig, M. Pápai, Z. Németh, R. Hartsock, W. Liang, J. Zhang, R. Alonso-Mori, M. Chollet, J. M. Glownia, S. Nelson, D. Sokaras, T. A. Assefa, A. Britz, A. Galler, W. Gawelda, C. Bressler, K. J. Gaffney, H. T. Lemke, K. B. Møller, M. M. Nielsen, V. Sundström, G. Vankó, K. Wärnmark, S. E. Canton, K. Haldrup, *Phys. Rev. Lett.* **2016**, *117*, 013002.
- [20] X. Zou, S. Hovmoller, P. Oleynikov, *Electron Crystallography – Electron Microscopy and Electron Diffraction, IUCr Texts on Crystallography, Vol. 16*, Oxford University Press, New York, **2011**.